Automated Adjustment of Aberration Correction in Scanning Confocal Microscopy

Han Woong Yoo*, Michel Verhaegen*, Martin E. van Royen†, and Georg Schitter§
*Delft Center for Systems and Control, Delft University of Technology,
Mekelweg 2, 2628 CD Delft, the Netherlands
Email: {h.w.yoo; m.verhaegen}@tudelft.nl
†Department of Pathology, Josephine Nefkens Institute, Erasmus Medical Center,
P.O. Box 2040, 3000 CA Rotterdam, the Netherlands
Email: m.vanroyen@erasmusmc.nl,
§Automation and Control Institute, Vienna University of Technology,
Gusshausstr. 27-29, 1040 Vienna, Austria
Email: schitter@acin.tuwien.ac.at

***Abstract*—This contribution demonstrates an automated adjustment of the coverslip correction collar in scanning confocal microscopy to compensate for aberrations caused by coverslip thickness mismatch. An axial image model is derived for filtering the measured axial image to improve the signal to noise ratio. To find the best collar alignment, 70 axial scans equally spaced over the actuation range are recorded and evaluated automatically. The axial scans reveal that different coverslips have a shift of the maximum intensity for optimal imaging along the collar angle. Correction quality such as the maximum intensity or sharpness of the image are examined and used to find the optimal adjustment. The proposed automated correction is demonstrated with two different coverslips and two biological specimen showing the improved resolution of the obtained confocal microscopy images.**

I. Introduction

Scanning confocal microscopy is widely used for biological studies as developing various fluorescence markers and techniques [1]. One of the main advantages of scanning confocal microscopy is the capability of sectioning the specimen, which enables three dimensional (3D) imaging. The maximum resolution of the microscope is given by the diffraction limit, depending on the numerical aperture of the objective lens and the wavelength of the excitation laser. However, this diffraction limited resolution is hardly obtained in practical microscopy due to various aberrations caused by the optical structure of the specimen, leading to a degenerated image.

One common aberration occurring in optical microscopy is the spherical aberration, as shown in Fig. 1, which is induced by the thickness variation of the coverslip, also called coverglass, a thin transparent plate to fix a specimen to the microscope slide and protect the specimen from external influences. Due to limited production precision, thickness variations of these coverslips are unavoidable. To cope with the aberrations some microscope manufacturers provide an objective lens with a coverslip correction collar that allows adjustment of a lens block in the objectives. A manufacturer of confocal microscopes recommends users to maximize the intensity of the interface reflection between the coverslip and specimen to find the best adjustment [2]. *Schwertner et al.* [3] define correction quality measures of these reflections of the clear interface without any specimen, which are $\mathcal{L}_p$ norms, e.g. image sharpness if $p = 2$, $\mathcal{L}_2$ [4], and find the optimal adjustment by Gaussian fitting. The manual adjustments, however, may be difficult and imprecise for users to search for the optimal correction. Additionally, finding a clear interface spot in a mounted specimen may be impractical, if available at all.

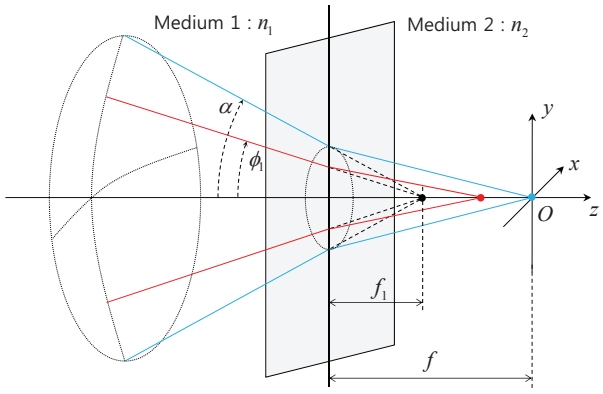

Fig. 1. Geometrical optics interpretation of the spherical aberrations caused by focusing a beam through two media ($n_2 > n_1$). The designed focal point of the lens in medium 1 (black dot) is diverged into two foci (red and blue dots), leading to image degradation.

This paper presents an automated correction of aberrations due to coverslip thickness mismatch by means of a motor driven correction collar (Section II). In Section III, an axial image model is derived to design a filter for improving the signal to noise ratio (SNR) of the measured images. A sequence of axial images is recorded and analyzed, and the optimal correction collar adjustment is obtained in terms of the selected correction quality measure in Section IV. Section V presents experimental results, demonstrating the improved image resolution of fluorescence images obtained by the automatically adjusted confocal microscope.

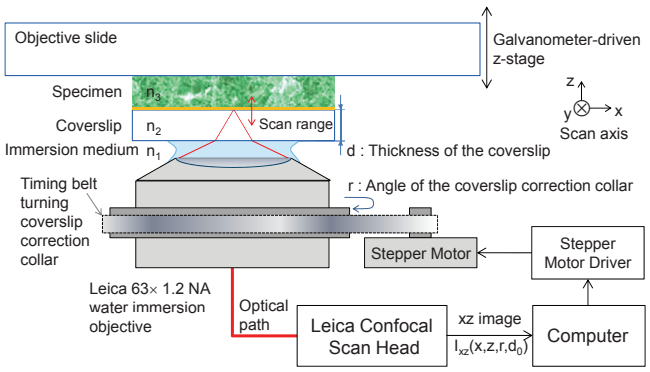

Fig. 2. Automated adjustment system for coverslip thickness mismatch correction.

II. System Description

Fig. 2 illustrates the overall structure of the automatic coverslip thickness mismatch correction system. An excitation laser ($488nm$, Ar laser) is collimated by an objective lens (HCX PL λ_{BL} APO $63\times$ 1.20NA water immersion, Leica Microsystems, Mannheim, Germany). The reflections between the coverslip and specimen are collected by the same objective lens, and detected by the photo multiplier tube (PMT) with the wavelength window from $485\mu m$ to $491\mu m$ in the confocal scanhead (DMI6000, TCS SP5, Leica Microsystems). For obtaining axial scans, the specimen slide is moved by a galvanometer driven z-stage (Super Z-Galvo Stage, Leica Microsystems). The axial images are recorded by a computer controlling the microscope. To actuate the coverslip correction collar, a stepper motor (15HS-012, Mclennan Servo Supplies Ltd., Surrey, United Kingdom) driven by a pulse generator (Stellaris Stepper Motor Reference Design Kit, Texas Instruments, Dallas, TX, USA) adjusts the angle of the coverslip correction collar through a timing belt with a gear ratio of $1/6$, providing a resolution of $0.33°$/step over the full range of $115°$ of the correction collar.

III. Axial Image Model

Imaging with coverslip mismatch can be modeled as imaging through two different media as shown in Fig. 1, where n_1 is the reflective index of the immersion media, and n_2 is that of the coverslip [1], [5]–[8]. An axial scan model that is based on an aberrations model in *Török et al.* [6] is derived for the matched filter design (cf. Section IV). The imaging intensity of a uniform reflective plane in confocal microscopy depends on the point spread function (PSF) and is given as follows [9],

$$I(x,y,z,f) = k^{-2}|\zeta|^2 \Omega I_{\mathcal{L}} \mathrm{PSF}(2\gamma z, f)\Big|_{x=y=0}, \qquad (1)$$

where x, y, and z are the coordinates at the imaged point as depicted in Fig. 1. $\mathrm{PSF}(z,d)\Big|_{x=y=0}$ denotes the one dimensional point spread function along the z axis through two media, and f denotes nominal focal depth in the second medium, the distance from the media interface to the nominal focal point. f equals to γf_1 with $\gamma = \frac{n_2}{n_1}$ and the designed focal point f_1 of the lens in medium 1. The wave vector k, reflectance ζ at the interface, a solid angel Ω of the aperture pupil as seen from either the object or image plane, and illumination intensity $I_{\mathcal{L}}$ at pupil are assumed constant.

Applying the Debye approximation [6], the axial PSF with aberrations of a linearly polarized light source is obtained as follows,

$$\mathrm{PSF}(z,f)\Big|_{x=y=0} = A^2 I_0(z,f)\bar{I}_0(z,f), \qquad (2)$$

where I_0 denotes a diffraction integral (see Eqn. 3), and $\bar{I}_0$ denotes the complex conjugate of I_0. A is a constant amplitude factor determined by focal length of the lens *in vacuo* and the wavenumber of the first medium. The other diffraction integrals of I_1 and I_2 in [6] equal 0 since the axial PSF, $x = y = 0$, corresponds $\phi_p = 0$ and the optical coordinate v is 0. The diffraction integral can be simplified as follows,

$$I_0(z,f) = \int_{\cos\alpha}^{1} F_0(\beta) e^{ik_0\Psi(\beta,f,z)} d\beta, \qquad (3)$$

where

$$F_0(\beta) = 2\sqrt{\beta^3}\left(\frac{1}{\eta(\beta)+\beta} + \frac{\gamma^{-2}\eta(\beta)}{\beta+\gamma^{-2}\eta(\beta)}\right), \qquad (4)$$

$$\Psi(\beta,f,z) = n_1\left\{f\left(\eta(\beta)-\beta\right) + z\eta(\beta)\right\}, \qquad (5)$$

$$\eta(\beta) = \sqrt{\beta^2+\gamma^2-1}, \qquad (6)$$

with $\beta = \cos\phi_1$ corresponding to the radial coordinate in the pupil plane (back focal plane). As shown in Fig. 1, ϕ_1 is the incident angle of the original focal point neglecting the refraction at the second medium, α is the maximum angle of ϕ_1, which is determined by the numerical aperture (NA) of the objective lens and the refractive index of the immersion medium n_1. $\Psi(\beta,f,z)$ is called the aberration function, representing the wavefront along the radial coordinate β at the axial position z with nominal focal depth f in the second medium. The aberration function Ψ can only represent spherical aberrations since Ψ is solely dependent on the radial coordinate, not on the angular coordinate.

From (3), it is observed that the nominal focal depth through the second medium influences the amplitude of the spherical aberration function Ψ. Considering the role of a coverslip correction collar, it should compensate this nominal focal depth at the reflective surface between coverslip and specimen by adjusting its angle, r. A linear relation between the adjustment r and the thickness of the coverslip d is assumed. Then, the nominal focal depth can be rewritten as

$$f = d_0 + br + \gamma z, \qquad (7)$$

where b denotes the coefficient of the correction collar in $\mu m/^\circ$ and d_0 is the residual mismatch in terms of nominal focal depth in the second medium at $r = 0$ and $z = 0$, where the maximum intensity is obtained along the axial axis z. The term γz reflects the displacement of the nominal focal depth in the second medium due to the shift of z position by the galvanometer-driven z-stage in Fig. 2. Substituting (7) into

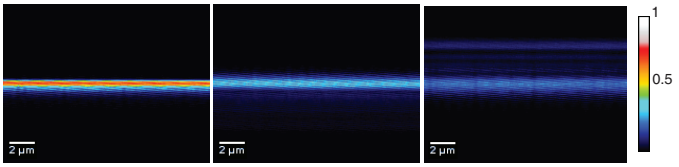

(a) Optimum (b) -33° off (c) $+33^\circ$ off

Fig. 3. Raw axial image of the reflection from the coverslip without specimen at (a) optimal correction, (b) -33° and (c) 33° off from optimal correction. The reflection of the coverslip is represented by the bright line at the center of the images, and is the brightest at optimum correction.

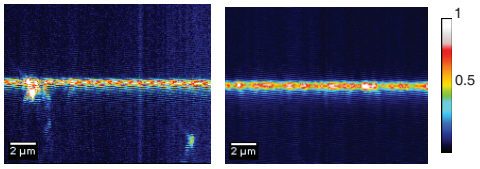

(a) w/ specimen #1 (b) w/ specimen #2

Fig. 4. Raw axial image of the reflection from (a) the coverslip with a specimen of Convallaria majalis rhizome, specimen #1, (b) the coverslip with a specimen of MEFs, specimen #2. The fluctuation of reflection intensity and additional reflections due to the specimen are observed.

(1), the xz image recorded by the microscope can be modeled as

$$I_{xz}(x,z,r,d_0) = k^{-2}|\zeta|^2 \Omega I_{\mathcal{L}} \mathrm{PSF}(z, d_0 + br + \gamma z)\Big|_{x=y=0}, \tag{8}$$

where $\mathrm{PSF}(\cdot,\cdot)$ is defined in (2) and (3). Considering the gain and offset of the detector, (8) can be rewritten as

$$\tilde{I}_{xz}(x,z,r,d_0) = K_g\Big\{I_{xz}(x,z,r,d_0) + v(x,z)\Big\} + K_{off}(r), \tag{9}$$

where K_g and K_{off} denote gain and offset of the detector. The term $v(x,z)$ represents the noise in the image such as dark current and readout noise [10].

Fig. 3 illustrates the axial images of the reflection from the coverslip-water-interface without a biological specimen at (a) optimal correction, (b) -33° and (c) 33° off from optimal correction. 33° corresponds to $16\mu m$ thickness mismatch in the coverslip. The reflection is brightest at the optimum and an interference pattern is observed when a mismatch is given. The axial image model in (9) explains this interference pattern from the amount of spherical aberrations and coverslip thickness mismatch.

Fig. 4 shows the axial images of the reflection from a coverslip with (a) a Convallaria majalis rhizome, and (b) a fixed mouse embryonic fibroblasts (MEFs, cf. Section V). It shows that an xz image has x dependency, in reality, not only due to the noise but also due to a nonuniform reflective surface along x, $\zeta(x)$, mainly caused by refractive index fluctuations of contacts of mounted specimen. An image processing algorithm, which provides a uniform representation over the entire x-range, is discussed in the following section.

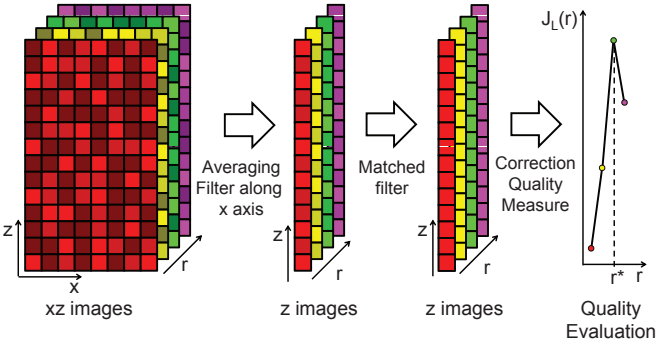

Fig. 5. Adjustment procedure of the proposed system. Each smallest square represents a pixel of the image, the color (red, yellow, green, violet) in the pixel means different collar adjustments r, and noise is shown as a shade of the color in the pixel. After recording an xz image at each adjustment r, each xz image is compressed into a z image vector by averaging, and a matched filter reduces the high frequency noise of each z image. The best adjustment r^* is obtained by searching the maximum of the correction quality is evaluated from each filtered z image.

IV. Automated Adjustments of Coverslip Thickness Mismatch

The overall procedure to find the best adjustment from the noisy xz images is illustrated in Fig. 5. 70 xz images ($41\mu m \times 41\mu m$, 512×512 pixels) equally spaced along the collar's full angular range of 115° are recorded by the microscope, which is regarded as a sufficient number of images to describe the aberration function of (5). For each xz image, an averaging filter along the x axis is applied generating a one dimensional z image with r as parameter. Then a matched filter is applied to reduce high spatial frequency noise. The correction quality of each correction angle is evaluated based on the maximum intensity and the sharpness of each z image.

A. Noise reduction filters and image processing

An averaging filter and a matched filter [11] are applied to improve the SNR of the measured axial image. The filtered image can be written as

$$I_h(z,r,d_0) = \left(\frac{1}{2x_m}\int_{-x_m}^{x_m} \tilde{I}_{xz}(x,z,r,d_0)dx\right) * h_m(z), \tag{10}$$

where x_m denotes a half of the averaging range of the x axis and $*$ is the convolution operator. For every xz image, an averaging filter is applied along the x axis reducing the noise term $v(x,z)$ of the image (9) and reform each xz image into a z image vector with a parameter r because the ideal axial image is independent of x. A matched filter $h_m(z)$ is based on the axial image model without mismatch, $h_m(z) = \mathrm{PSF}(2\gamma z, 0)\Big|_{x=y=0}$, using the fact that the maximum spatial frequency of axial images is bounded by the diffraction limit of the optical system, and is independent of the coverslip mismatch.

To compare them, the obtained z images are aligned at the center $z = 0$ by their maximum intensity position, and cropped symmetrically by a distance z_m. An offset rejector subtracts the slow drift and offset $K_{off}(r)$ of the detector, which is

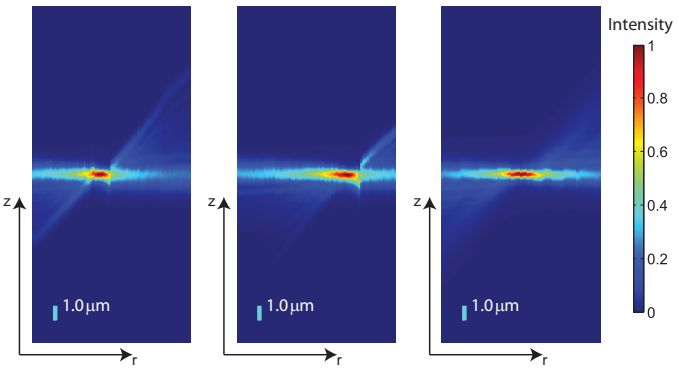

(a) Coverslip #1 (b) Coverslip #2 (c) Simulation

Fig. 6. rz image of a coverslip with thickness (a) $150\mu m$, (b) $170\mu m$, and (c) simulation.

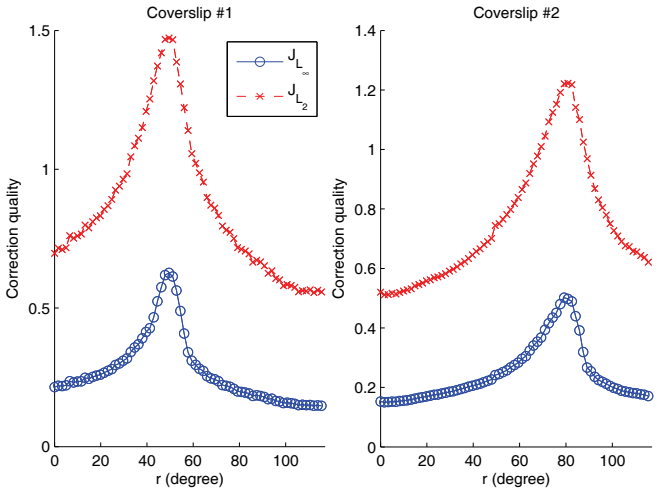

Fig. 7. Correction quality measures of two coverslips without specimen. The blue solid lines with o marks represent the maximum intensity $J_{\mathcal{L}_\infty}$, and the red dashed lines with x marks represent the sharpness $J_{\mathcal{L}_2}$ as a function of r.

obtained by the minimum mean intensity at either ends of the respective z image.

To illustrate the evolution of the z image along r, an rz image is generated by stitched the z image vectors along the collar angle r. Fig. 6 illustrates three rz images, two measured rz image of two different coverslips with a thickness of approximately $150\mu m$ (coverslip #1) and $170\mu m$ (coverslip #2) respectively, and the rz image obtained by simulation of (9) with $v(x,z)=0$. It is clearly seen that both measurements and the simulation match well and that the highest intensity and the sharpest z image can be defined as the optimal adjustment. It also illustrates that the optimal adjustment is shifted in r due to the coverslip thickness variation. The spreading pattern of the z image vector is independent of the thickness variation but dependent on the misalignment from the optimal adjustment as also observed in the simulation.

B. Correction quality measures and optimal correction

From the observation in the rz image, two correction quality measures are used to evaluate each z image as a function of r, according to [3],

$$J_{\mathcal{L}_\infty}(r,d_0) = \lim_{p\to\infty}\left(\int_{-z_m}^{+z_m} I_h^p(z,r,d_0)dz\right)^{1/p}, \quad (11)$$

$$J_{\mathcal{L}_2}(r,d_0) = \left(\int_{-z_m}^{+z_m} I_h^2(z,r,d_0)dz\right)^{1/2}. \quad (12)$$

The maximum intensity $J_{\mathcal{L}_\infty}$ corresponds to the Strehl ratio of the imaging system, which is defined as a ratio between the maximum intensity with and without aberrations. It is easily obtained by the cross section of the rz image at the center. $J_{\mathcal{L}_2}$ is known as a measure of image sharpness [4].

Each correction quality measure as a function of the correction collar angle r is illustrated in Fig. 7 for the two measured coverslips. Both correction quality measures have the same or similar maxima. For coverslip #1 the maxima of both measures are the same and coverslip #2 has a slight difference of only $1.65°$ between the two maxima. After identifying the collar adjustment angle r for the optimal intensity or sharpness, the new correction system automatically adjusts the correction collar to this value of r with the stepper motor.

V. Imaging Example

The proposed automated adjustment system is demonstrated by imaging two biological specimen with the optimally adjusted microscope and without automated adjustment of the aberration correction. The first specimen is a Convallaria majalis (Lily-of-the-Valley) rhizome with concentric vascular bundles (Leica Microsystems) [12]. Its chloroplasts have been stained with fluorescein isothiocyanate (FITC). The cell wall shows autofluorescence. An Ar laser with a wavelength of $488nm$ and a diode pumped solid state (DPSS) laser with a wavelength of $561nm$ are used to excite FITC and autofluorescence respectively. To obtain the optimal setting of the correction collar, axial images of the reflection of the Ar laser are used and analyzed by the methods described in Section IV. The fluorescence of both dyes is recorded with the corresponding PMTs simultaneously.

Fig. 8 illustrates the benefits of the noise filters to the rz images and corresponding correction quality measures without any noise filter, only with an averaging filter, and with averaging and matched filters, as discussed in Section IV. The correction measures are normalized by scaling their maxima and the minima to 1 and 0 respectively for the comparison. Filtering smoothes the noisy rz images and many local minima in the quality measures are reduced. The filters are thus advantageous to determine the optimal correction. The maximum of $J_{\mathcal{L}_\infty}$ and $J_{\mathcal{L}_2}$ are the same at $80.85°$ when both filters are applied, while those in the other cases differ, occurring at $82.5°$ and $80.85°$.

For the comparison, the system is adjusted to the optimal r as well as $49.5°$ off from the optimal r, corresponding to a coverslip thickness mismatch of $24\mu m$. Considering about $40\mu m$ thickness variation in the standard coverslip number 1,

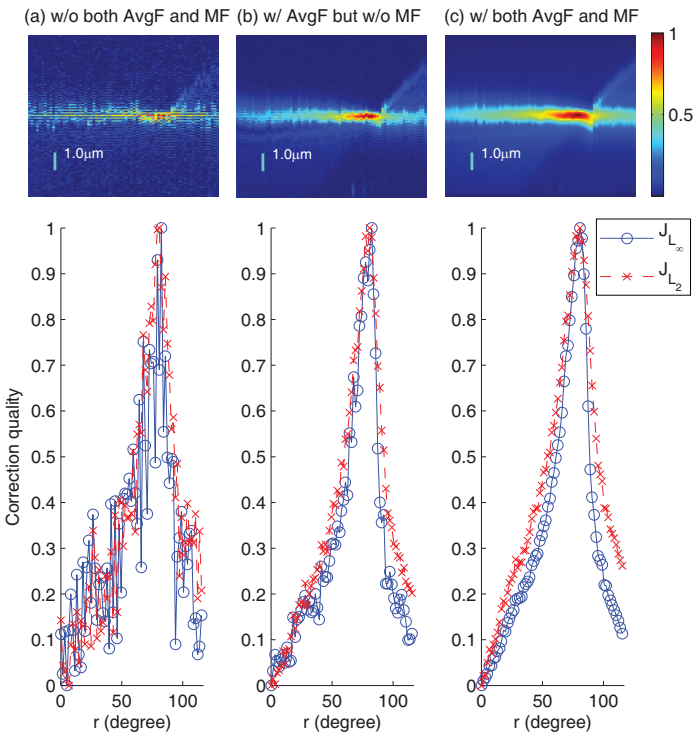

Fig. 8. rz image and corresponding normalized correction quality measures of the Leica standard slide of Convallaria majalis rhizome in case of (a) without both averaging filter and matched filter, (b) with averaging but without matched filter, (c) with both averaging filter and matched filter. The averaging size, $2x_m$, is 50 pixels, $4\mu m$. As filtering is applied, the correction quality curve gets smoother along the ring position as can be seen in rz figure.

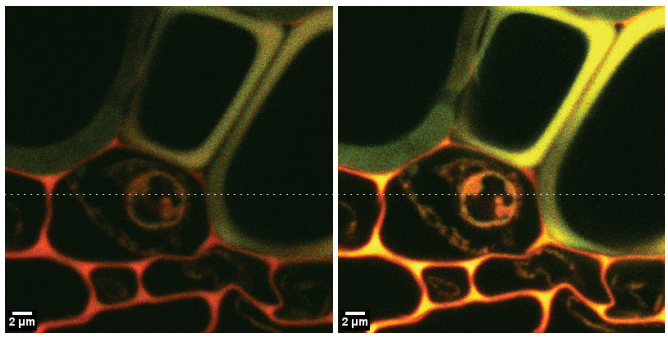

(a) 49.5° off from optimum (b) optimum

Fig. 9. xy fluorescence images of Convallaria majalis Rhizome with chloroplast (FITC, Green Hot LUT), cell wall (autofluorescence, Red Hot LUT). The image of both fluorephores gets brighter and sharper at the optimal collar adjustment angle.

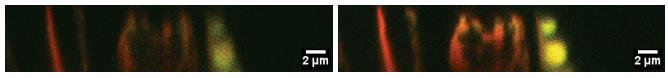

(a) 49.5° off from optimum (b) optimum

Fig. 10. yz fluorescence images of Convallaria majalis rhizome with chloroplast (FITC, Green Hot LUT), cell wall (autofluorescence, Red Hot LUT). These are the sectional images at the dotted lines in Fig. 9 (a and b).

ranging $130\mu m - 170\mu m$, this is a valid comparison. The 3D images of the specimen in the uncompensated and optimally adjusted cases are recorded by stacking 127 xy image layers

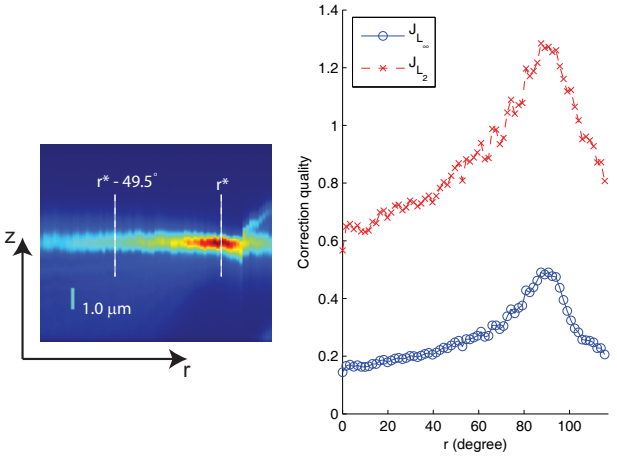

(a) rz image (b) Correction quality

Fig. 11. Measured coverslip reflection of the slide of a fixed mouse embryonic fibroblasts (MEFs). Fluorescence images are recorded at the optical correction r^* and at $-49.5°$ mismatch as indicated by dashed line in rz image.

maintaining the same z voxel height with xy voxel width. The image is aligned based on a cross-correlation maximization between two 3D images to compare the same position as well as to remove the effect of defocus by a different z position. The detector parameters and laser power are fixed while recording both the 3D images.

Fig. 9 and Fig. 10 show a lateral xy and its sectional yz image slice of the 3D images of the Convallaria majalis rhizome with (a) the uncompensated microscope and (b) the optimally adjusted correction collar. The optimum correction provides a bright and sharp image by minimizing the spherical aberrations while the details in the uncompensated images are blurred. The image degradation is more significant in the axial images (Fig 10) shown by the elongated spherical structure (green) and rapidly losing its details along the depth axis.

The second specimen are fixed mouse embryonic fibroblasts (MEFs) [13]. The cytoskeleton of MEFs is visualized by means of immunofluorescent labeling of beta-tubulin (Alexa488) and with a chromatin staining (DAPI) that are excited by a $488nm$ Ar laser and a $405nm$ diode laser respectively. Contrary to the structures in Convallaria majalis rhizome, beta-tubulin in MEFs has an approximately $24nm$ diameter hollow cylindrical structure [14], which is smaller than the diffraction limit of the confocal microscope and is regarded as a useful indicator with a high sensitivity to aberrations. As the previous specimen, the optimum is obtained by the reflection of the Ar laser with the method proposed in Section IV.

Fig. 11 shows the obtained rz image and the corresponding correction quality measures of the specimen with the averaging size of 200 pixels, $16\mu m$. The overall features of Fig. 11 resemble Figs. 6 and 7, except that Fig. 11 has higher noise as in Fig. 8. The optimum adjustment is chosen as $89.1°$, which is the mean value of the angles of maximum $J_{\mathcal{L}_\infty}$ and $J_{\mathcal{L}_2}$ at $90.75°$ and $87.45°$, respectively. As previous, the system is

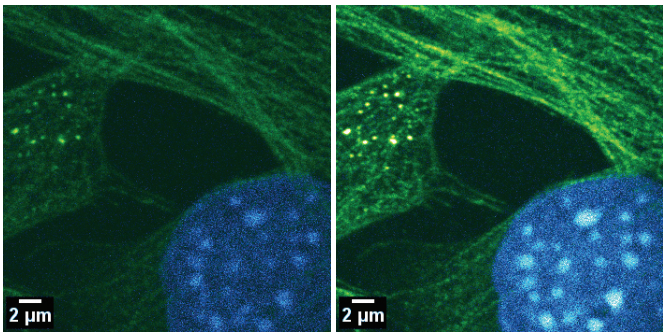

(a) $49.5°$ off from optimum (b) optimum

Fig. 12. xy fluorescence images of fixed mouse embryonic fibroblasts with chromatin (DAPI, Cyan Hot LUT), beta-tubulin (Alexa488, Green Hot LUT). The image get brighter and sharper at the optimal collar adjustment.

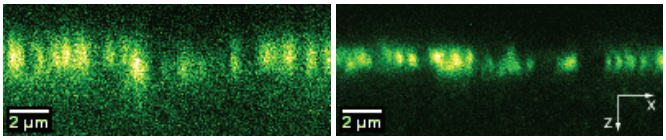

(a) $49.5°$ off from optimum (b) optimum

Fig. 13. xz fluorescence image of the beta-tubulin (Alexa488). Both lateral x and axial z resolution is the best at the optimal adjustment, resulting in the smallest PSF.

adjusted $49.5°$ off from the optimum, denoting the case of the uncompensated microscope.

Fig. 12 shows xy fluorescence images for (a) the uncompensated microscope and (b) the optimally adjusted correction collar. In both images the two fluorescence markers are recorded simultaneously with each PMT. Fig. 13 shows xz fluorescence images of the beta-tubulin with an adapted gain and offset of the PMTs to compare the resolution without the brightness and contrast difference. It is clearly observed that the proposed automated adjustment minimizes spherical aberrations, resulting in the smallest PSF, the highest intensity, and a sharp lateral as well as axial resolution of the confocal microscope.

VI. Conclusion

In this paper, an automated adjustment of the coverslip correction collar in scanning confocal microscopes is proposed. A method for noise reduction in the axial image is derived from an axial image model. The best correction angle is obtained based on correction quality measures, such as the maximum intensity and sharpness of the image. The proposed automated adjustment is demonstrated with two different coverslips and two biological specimen, Convallaria majalis rhizome and fixed mouse embryonic fibroblasts. Confocal fluorescence imaging examples illustrate the benefits of the proposed automatic adjustment, enabling precise localization and signal detection in biological fluorescence imaging by minimizing spherical aberrations. The proposed automation of the aberration correction allows confocal microscope users to consistently obtain bright and high contrast images and to save their effort to consider the spherical aberrations in the specimen preparation.

Future development of this work is focussed on the automatic compensation of the aberrations in general, including non-spherical aberrations, in the scanning confocal microscopy by means of adaptive optics. This research finally aims to provide confocal microscopy with minimal aberrations for a wide range of specimen, supporting high resolution imaging for biological and medical science research.

Acknowledgment

This research has been supported by the Integrated Smart Microscopy project in the Smart Optics Systems program of Technologiestichting STW, the Netherlands. The authors would like to thank Jeffrey van Haren for providing a biological specimen, and Wiggert A. van Cappellen, and Adriaan B. Houtsmuller for fruitful discussions.

References

[1] J. B. Pawley, Ed., *Handbook of biological confocal microscopy*, 3rd ed. Springer Science Business Media, 2006.
[2] *Glycerol Objective*, Leica microsystems, April 2004.
[3] M. Schwertner, M. J. Booth, and T. Wilson, "Simple optimization procedure for objective lens correction collar setting," *Journal of microscopy*, vol. 217, no. 3, pp. 184–187, 2004.
[4] L. P. Murray, J. C. Dainty, and E. Daly, "Wavefront correction through image sharpness maximisation," *Proc. SPIE Opto-Ireland 2005: Imaging and Vision*, vol. 5823, no. 40.
[5] S. Hell, G. Reiner, C. Cremer, and E. H. K. Stelzer, "Aberrations in confocal fluorescence microscopy induced by mismatches in refractive index," *Journal of microscopy*, vol. 169, no. 3, pp. 391–405, 1993.
[6] P. Török, P. Varga, Z. Laczik, and G. R. Booker, "Electromagnetic diffraction of light focused through a planar interface between materials of mismatched refractive indices: an integral representation," *J. Opt. Soc. Am A*, vol. 12, no. 2, pp. 325–332, 1995.
[7] M. J. Booth, M. A. A. Neil, and T. Wilson, "Aberration correction for confocal imaging in refractive-index-mismatched media," *Journal of microscopy*, vol. 192, no. 2, pp. 90–98, 1998.
[8] M. J. Booth and T. Wilson, "Refractive-index-mismatch induced aberrations in single-photon and two-photon microscopy and the use of aberration correction," *Journal of Biomedical Optics*, vol. 6, no. 3, pp. 266–272, 2001.
[9] J. Mertz, Ed., *Introduction to Optical Microscopy*, 1st ed. Roberts and company publisher, 2009.
[10] Q. Wu, F. A. Merchant, and K. R. Castleman, *Microscope image processing*, 1st ed. Academic Press, 2008.
[11] H. L. V. Trees, *Detection, Estimation, and Modulation Theory, Part I.* Wiley-Interscience, 2001.
[12] *Leica TCS SP5 User Manual*, Leica Microsystems, order No.: 156500002.
[13] K. Drabek, M. van Ham, T. Stepanova, K. Draegestein, R. van Horssen, C. L. Sayas, A. Akhmanova, T. ten Hagen, R. Smits, R. Fodde, F. Grosveld, and N. Galjart, "Role of CLASP2 in Microtubule Stabilization and the Regulation of Persistent Motility," *Current Biology*, vol. 16, no. 22, pp. 2259–2264, 2006.
[14] C. Conde and A. Cáceres, "Microtubule assembly, organization and dynamics in axons and dendrites," *Nature Reviews Neuroscience*, vol. 10, no. 5, pp. 319–332, 2009.